

Pose estimation by extended Kalman filter using noise covariance matrices based on sensor output

AYUKO SAITO (✉ saito@cc.kogakuin.ac.jp)

Kogakuin Daigaku <https://orcid.org/0000-0002-1675-8049>

Satoru Kizawa

National Institute of Technology Akita college

Yoshikazu Kobayashi

National Institute of Technology Akita college

Kazuto Miyawaki

National Institute of Technology Akita college

Research Article

Keywords: Kalman filter, Motion sensor, Noise covariance matrix, Pose estimation, Sensor fusion

Posted Date: September 14th, 2020

DOI: <https://doi.org/10.21203/rs.3.rs-29523/v2>

License:  This work is licensed under a Creative Commons Attribution 4.0 International License.

[Read Full License](#)

Version of Record: A version of this preprint was published on October 19th, 2020. See the published version at <https://doi.org/10.1186/s40648-020-00185-y>.

RESEARCH

Pose estimation by extended Kalman filter using noise covariance matrices based on sensor output

Ayuko SAITO^{1*}, Satoru KIZAWA², Yoshikazu KOBAYASHI² and Kazuto MIYAWAKI²

Abstract

This paper presents an extended Kalman filter for pose estimation using noise covariance matrices based on sensor output. Compact and lightweight nine-axis motion sensors are used for motion analysis in widely various fields such as medical welfare and sports. A nine-axis motion sensor includes a three-axis gyroscope, a three-axis accelerometer, and a three-axis magnetometer. Information obtained from the three sensors is useful for estimating joint angles using the Kalman filter. The extended Kalman filter is used widely for state estimation because it can estimate the status with a small computational load. However, determining the process and observation noise covariance matrices in the extended Kalman filter is complicated. The noise covariance matrices in the extended Kalman filter were found for this study based on the sensor output. Postural change appears in the gyroscope output because the rotational motion of the joints produces human movement. Therefore, the process noise covariance matrix was determined based on the gyroscope output. An observation noise covariance matrix was determined based on the accelerometer and magnetometer output because the two sensors' outputs were used as observation values. During a laboratory experiment, the lower limb joint angles of three participants were measured using an optical 3D motion analysis system and nine-axis motion sensors while participants were walking. The lower limb joint angles estimated using the extended Kalman filter with noise covariance matrices based on sensor output were generally consistent with results obtained from the optical 3D motion analysis system. Furthermore, the lower limb joint angles were measured using nine-axis motion sensors while participants were running in place for about 100 seconds. The experiment results demonstrated the effectiveness of the proposed method for human pose estimation.

Keywords: Kalman filter, Motion sensor, Noise covariance matrix, Pose estimation, Sensor fusion

1	18	
2	Introduction	19
3	Compact and lightweight nine-axis motion sensors	20
4	have been developed through advances in micro-	21
5	electromechanical systems technology; they have	22
6	come to be used for motion analysis in widely various	23
7	fields [1-8]. The nine-axis motion sensors are	24
8	applicable both indoors and outdoors because of their	25
9	portability. Several experiments have been conducted	26
10	to measure the motion of a skier gliding down a slope	27
11	and jumping off a hill using motion sensors [9,10].	28
12	The nine-axis motion sensors include a three-axis	29
13	gyroscope, a three-axis accelerometer, and a three-	30
14	axis magnetometer. Using information obtained from	31
15	the motion sensors, several sensor fusion algorithms	32
16	have been proposed for pose estimation: as one	33
17	example, a sensor fusion algorithm that can correct	34
	35	gyroscope drift using information obtained from the
	36	other two sensors has been used for human pose
	37	estimation during daily activities and exercise [11-13].
	38	Furthermore, a sensor fusion algorithm able to correct
	39	the magnetometer output using information obtained
		from a gyroscope has been used for pose estimation
		in a variable magnetic field [14,15]. The Kalman filter
		[16-20] and the complementary filter [21-25] are
		some pose estimation methods using sensor fusion.
		The Kalman filter estimates the system
		state with a small computational load. Nevertheless,
		determining the process and observation noise
		covariance matrices in the Kalman filter is
		complicated. For a case in which the process and
		observation noise covariance matrices are time-
		invariant, the estimation accuracy might decrease if
		the sensor output noise increases. Moreover, the noise
		of the sensor output might vary because of long-term
		measurements. For that reason, adjusting the noise
		covariance matrices based on sensor output is
		important.

*Correspondence: saito@cc.kogakuin.ac.jp

¹ Department of Mechanical Science and Engineering, Kogakuin University, Hachioji, Tokyo, Japan

Full list of author information is available at the end of the article

1 To estimate the lower limb joint angles for 55
 2 this study, a method was devised to determine the 56
 3 process and observation noise covariance matrices in 57
 4 the extended Kalman filter based on sensor output. 58
 5 The postural change appears in the gyroscope output 59
 6 because the rotational motion of the joints produces 60
 7 human movement. Therefore, the process noise 61
 8 covariance matrix was set based on the gyroscope 62
 9 output. When the accelerometer output increased, the 63
 10 observation noise covariance matrix was set to 64
 11 increase. The observation noise covariance matrix 65
 12 was also set to increase when the magnetometer 66
 13 output drastically changed. During a laboratory 67
 14 experiment, the lower limb joint angles of three 68
 15 participants were measured using an optical 69
 16 motion analysis system and nine-axis motion sensors 70
 17 while the participants were walking. Several studies 71
 18 have demonstrated that an optical 3D motion analysis 72
 19 system measured human movement with high 73
 20 accuracy. Therefore, the system is used for verifying 74
 21 the pose estimation accuracy in widely diverse fields 75
 22 [26-29]. We verified the accuracy of the proposed 76
 23 method by comparing its results to those of an optical 77
 24 3D motion analysis system. Furthermore, the lower 78
 25 limb joint angles were measured using nine-axis 79
 26 motion sensors while the participants were running in 80
place. Finally, the effectiveness of the proposed 81
 27 method was verified using experiment results. 82
 28

30 **Measurement method** 79
 31 **Definition of roll-pitch-yaw** 80
 32 The 3D posture of the sensor is represented by the roll 81
 33 angle (ϕ) around the x-axis, the pitch angle (θ) 82
 34 around the y-axis, and the yaw angle (ψ) around the 83
 35 z-axis. The reference coordinate system is a right- 84
 36 handed system with a vertical z-axis. The 85
 37 counterclockwise rotation is defined as positive. The 86
 38 reference coordinate system and the definition of the 87
 39 joint angles are presented in Fig. 1. 88

40
 41 **Roll-pitch-yaw calculation**
 42 For this study, Euler angles (roll, pitch, and yaw) were 89
 43 calculated using nine-axis motion sensors. The nine- 89
 44 axis motion sensor (SS-WS1792; Sports Sensing Co., 90
 45 Ltd.) used for this study includes a three-axis 90
 46 gyroscope (± 1500 dps), a three-axis accelerometer 90
 47 (± 16 G), and a three-axis magnetometer (± 10 Gauss). 90
 48 The $38 \times 53 \times 11$ mm sensor weighs 30g.

49 The initial roll and pitch angles were
 50 calculated using the accelerometer output at rest 91
 51 [30,31]. The relation between the acceleration sensor 92
 52 output and the gravitational acceleration in the 92
 53 reference coordinate system is expressed using Eq. 93
 54 (1) because the accelerometer measures only the 94

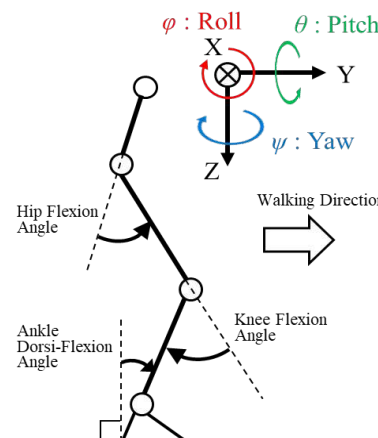


Fig. 1 Definition of the lower limb joint angles and the reference coordinate system.

gravitational acceleration while at rest:

$${}^iA = ({}^oR_i)^T {}^oA, \quad (i = 1, 2, 3, 4) \quad (1)$$

where

$${}^iA = \begin{bmatrix} {}^iA_x \\ {}^iA_y \\ {}^iA_z \end{bmatrix}, \quad {}^oA = \begin{bmatrix} 0 \\ 0 \\ g \end{bmatrix},$$

Therein, iA denotes the accelerometer output, oA represents the acceleration in the reference coordinate system, and g stands for gravitational acceleration. For the experiment, sensors 1, 2, 3, and 4 were placed respectively on the waist, left thigh, left shank, and left foot. In addition, the rotational matrix from the sensor coordinate system to the reference system oR_i is the following:

$$\begin{aligned} {}^oR_i &= \begin{bmatrix} \cos i\psi & -\sin i\psi & 0 \\ \sin i\psi & \cos i\psi & 0 \\ 0 & 0 & 1 \end{bmatrix} \cdot \begin{bmatrix} \cos i\theta & 0 & \sin i\theta \\ 0 & 1 & 0 \\ -\sin i\theta & 0 & \cos i\theta \end{bmatrix} \cdot \begin{bmatrix} 1 & 0 & 0 \\ 0 & \cos i\phi & -\sin i\phi \\ 0 & \sin i\phi & \cos i\phi \end{bmatrix}, \\ &\quad (2) \end{aligned}$$

Then, the accelerometer output iA is represented by substituting Eq. (2) into Eq. (1) as shown below:

1 $\begin{bmatrix} {}^iA_x \\ {}^iA_y \\ {}^iA_z \end{bmatrix} = \begin{bmatrix} -\sin {}^i\theta \cdot g \\ \cos {}^i\theta \sin {}^i\phi \cdot g \\ \cos {}^i\theta \cos {}^i\phi \cdot g \end{bmatrix}. \quad (3)$

2 3 The initial roll and pitch angles using Eq. (3) are:

5 ${}^i\phi_A = \text{atan}2 \frac{{}^iA_y}{{}^iA_z} \quad (-\pi < {}^i\phi_A < \pi) \quad (4)$

6 ${}^i\theta_A = \text{atan}2 \frac{-{}^iA_x}{\sqrt{{}^iA_y^2 + {}^iA_z^2}} \quad (-\pi < {}^i\theta_A < \pi) \quad (5)$

8 where iA_x , iA_y , and iA_z respectively denote the
9 accelerometer output for the x , y , and z axes. Therein,
10 ${}^i\phi_A$ and ${}^i\theta_A$ respectively denote the initial roll and pitch.

11 To correct the yaw angle, calculations
12 require the roll ${}^i\phi_A$, pitch ${}^i\theta_A$, and magnetometer
13 output as:

15 $\begin{bmatrix} {}^{c,i}m_x \\ {}^{c,i}m_y \\ {}^{c,i}m_z \end{bmatrix} = \begin{bmatrix} \cos {}^i\theta_A & \sin {}^i\phi_A \sin {}^i\theta_A & \cos {}^i\phi_A \sin {}^i\theta_A \\ 0 & \cos {}^i\phi_A & -\sin {}^i\phi_A \\ -\sin {}^i\theta_A & \sin {}^i\phi_A \cos {}^i\theta_A & \cos {}^i\phi_A \cos {}^i\theta_A \end{bmatrix} \cdot \begin{bmatrix} {}^i m_x \\ {}^i m_y \\ {}^i m_z \end{bmatrix}, \quad (6)$

16 17 where ${}^i m_x$, ${}^i m_y$, and ${}^i m_z$ respectively denote the
18 magnetometer outputs for the x , y , and z axes. Therein,
19 ${}^{c,i}m_x$, ${}^{c,i}m_y$, and ${}^{c,i}m_z$ respectively represent the
20 corrected magnetic field data for the x , y , and z axes.

21 The positive directions of ${}^{c,i}m_x$, ${}^{c,i}m_y$, and ${}^{c,i}m_z$ coincide
22 with those of each axis of the reference coordinate
23 system in Fig. 1. The x -axis pointed in the direction
24 of the azimuth at 112.5 degrees (east-southeast). The
25 y -axis pointed in the direction at the azimuth of 202.5
26 degrees (south-southwest) in the reference
27 coordinates.

28 29 The following equation is used for
30 calculating yaw:

32 ${}^i\psi_m = \text{atan}2 \frac{-{}^{c,i}m_y}{{}^{c,i}m_x} \quad (-\pi < {}^i\psi_m < \pi) \quad (7)$

33 34 where ${}^i\psi_m$ denotes the azimuth on the x - y plane of
35 the reference coordinates in Fig. 1.

36 37 The differential Euler angles in the
38 reference coordinate system are the following:

38 $\begin{bmatrix} {}^i\psi \\ {}^i\theta \\ {}^i\phi \end{bmatrix} = \begin{bmatrix} 0 & \sin {}^i\phi \sec {}^i\theta & \cos {}^i\phi \sec {}^i\theta \\ 0 & \cos {}^i\phi & -\sin {}^i\phi \\ 1 & \sin {}^i\phi \tan {}^i\theta & \cos {}^i\phi \tan {}^i\theta \end{bmatrix} \begin{bmatrix} {}^i\omega_x \\ {}^i\omega_y \\ {}^i\omega_z \end{bmatrix}, \quad (8)$

40 Therein, ${}^i\phi$, ${}^i\theta$, and ${}^i\psi$ respectively represent
41 the differential roll, pitch, and yaw angles; ${}^i\omega_x$,
42 ${}^i\omega_y$ and ${}^i\omega_z$ respectively stand for the gyroscope
43 output for the x , y , and z axes. Then the roll, pitch, and
44 yaw angles are calculated by substituting Eq. (8) into
Eq. (9):

46 $\begin{bmatrix} {}^i\psi \\ {}^i\theta \\ {}^i\phi \end{bmatrix}_{t+1} = \int \begin{bmatrix} {}^i\psi \\ {}^i\theta \\ {}^i\phi \end{bmatrix} dt + \begin{bmatrix} {}^i\psi \\ {}^i\theta \\ {}^i\phi \end{bmatrix}_t. \quad (9)$

Extended Kalman filter

State-space model

The roll, pitch, and yaw angles of each sensor placed
on the lower limb are estimated by the sensor fusion
using the extended Kalman filter. The nonlinear state
equation was developed using Eq. (9). The nonlinear
observation equation was developed using Eq. (7) and
the acceleration sensor output. The nonlinear state
and observation equations are shown respectively in
Eqs. (10) and (11):

60 ${}^i x_{t+1} = {}^i F({}^i x_t, {}^i \omega_t) + {}^i w_t, \quad (10)$

61 ${}^i y_t = {}^i H({}^i x_t) + {}^i v_t, \quad (11)$

where

$${}^i x_t = \begin{bmatrix} {}^i\psi \\ {}^i\theta \\ {}^i\phi \end{bmatrix}_t,$$

$${}^i F(x_t, \omega_t) = \begin{bmatrix} {}^i\psi_t + \sin {}^i\phi_t \sec {}^i\theta_t {}^i\omega_{y,t} \cdot Ts + \cos {}^i\phi_t \sec {}^i\theta_t {}^i\omega_{z,t} \cdot Ts \\ {}^i\theta_t + \cos {}^i\phi_t {}^i\omega_{y,t} \cdot Ts - \sin {}^i\phi_t {}^i\omega_{z,t} \cdot Ts \\ {}^i\phi_t + {}^i\omega_{x,t} \cdot Ts + \sin {}^i\phi_t \tan {}^i\theta_t {}^i\omega_{y,t} \cdot Ts + \cos {}^i\phi_t \tan {}^i\theta_t {}^i\omega_{z,t} \cdot Ts \end{bmatrix},$$

$${}^i y_t = \begin{bmatrix} {}^i\psi_m \\ {}^iA_{Sx} \\ {}^iA_{Sy} \\ {}^iA_{Sz} \end{bmatrix}_t, \quad {}^i H(x_t) = \begin{bmatrix} {}^i\psi_t \\ ({}^0R_i)^T \begin{bmatrix} 0 \\ 0 \\ g \end{bmatrix} \end{bmatrix},$$

In those equations, ${}^i\phi_t$, ${}^i\theta_t$, and ${}^i\psi_t$
respectively denote Euler angles of the sensor placed
on each lower limb segment, as estimated using the
extended Kalman filter. Ts stands for the sampling
time. In addition, ${}^i\omega_{x,t}$, ${}^i\omega_{y,t}$, and ${}^i\omega_{z,t}$

1 respectively denote the gyroscope outputs for the x, y ,
 2 and z axes. Also, ${}^iA_{S_x}$, ${}^iA_{S_y}$, and ${}^iA_{S_z}$
 3 respectively express the accelerometer output for the
 4 x , y , and z axes. Therein, iw_t and iv_t denote
 5 white noise.
 51

6 Yaw angle ${}^i\psi_m$, which was calculated
 7 using the magnetometer output, and the
 8 accelerometer output were used as the observation
 9 values in Eq. (11). Eq. (1) represents the relation
 10 between the accelerometer output and gravitational
 11 acceleration. Consequently, the right side of Eq. (1)
 12 was used in ${}^iH({}^ix_t)$ of the observation equation.
 13 Although the proportion of the centrifugal
 14 acceleration and the tangential acceleration in the
 15 accelerometer output would have increased during
 16 exercise, these acceleration components were
 17 processed as observation noise. In addition, ${}^i\psi_m$
 18 is a simple equation representing the relation
 19 between the magnetometer output and the yaw angle
 20 of the state values. Therefore, the yaw angle ${}^i\psi_t$ of
 21 the state value was used in ${}^iH({}^ix_t)$ of the
 22 observation equation.

23 The partial derivatives of ${}^iF({}^ix_t, {}^i\omega_t)$
 24 and ${}^iH({}^ix_t)$ are shown below:
 25

$$26 \quad {}^if({}^ix_t, {}^i\omega_t) = \frac{\partial {}^iF({}^ix_t, {}^i\omega_t)}{\partial {}^ix_t}, \quad (12)$$

$$27 \quad {}^iH({}^ix_t) = \frac{\partial {}^iH({}^ix_t)}{\partial {}^ix_t}. \quad (13)$$

28 Then, the prediction step [Eqs. (14) and
 29 (15)] and the filtering step [Eqs. (18)–(20)] are
 30 calculated using the nonlinear discrete-time system
 31 represented by Eqs. (10) and (11). Here, Eq. (16) and
 32 Eq. (17) are used for calculating the likelihood of the
 33 state-space model:
 34

$$37 \quad {}^ix_{t+1}^- = {}^iF({}^ix_t, {}^i\omega_t), \quad (14)$$

$$38 \quad {}^iP_{t+1}^- = {}^if_t {}^iP_t {}^if_t^T + {}^iQ_t, \quad (15)$$

$$39 \quad {}^iV_{t+1} = {}^iy_{t+1} - {}^iH({}^ix_{t+1}^-), \quad (16)$$

$$40 \quad {}^iB_{t+1} = {}^ih_{t+1} {}^iP_{t+1}^- {}^ih_{t+1}^T + {}^iR_t, \quad (17)$$

$$41 \quad {}^iK_{t+1} = {}^iP_{t+1}^- {}^ih_{t+1}^T \left({}^ih_{t+1} {}^iP_{t+1}^- {}^ih_{t+1}^T + {}^iR_t \right)^{-1}, \quad (18)$$

$$43 \quad {}^ix_{t+1} = {}^ix_{t+1}^- + {}^iK_{t+1} ({}^iy_{t+1} - {}^iH({}^ix_{t+1}^-)), \quad (19)$$

$$45 \quad {}^iP_{t+1} = (I - {}^iK_{t+1} {}^ih_{t+1}) {}^iP_{t+1}^-, \quad (20)$$

In those equations, iP represents the error covariance matrix, iV denotes the prediction error matrix, iB stands for the prediction error variance matrix, and iK denotes the Kalman gain. Therein, iQ and iR respectively denote the covariance matrices of process noise iw_t in the nonlinear state equation and observation noise iv_t in the nonlinear observation equation.

Noise covariance matrices based on sensor output

The process and observation noise covariance matrices in the extended Kalman filter were determined based on the state-space model dynamics and the sensor noise. The postural change appears in the gyroscope output because the rotational motion of the joints produces human movement. Consequently, the process noise covariance matrix was determined based on the gyroscope output as presented below:

$$66 \quad {}^iQ_t = \begin{bmatrix} {}^i\Omega_{\omega,t} & 0 & 0 \\ 0 & {}^i\Omega_{\omega,t} & 0 \\ 0 & 0 & {}^i\Omega_{\omega,t} \end{bmatrix}, \quad (21)$$

where

$$68 \quad {}^i\Omega_{\omega,t} = a \sqrt{{}^i\omega_{x,t}^2 + {}^i\omega_{y,t}^2 + {}^i\omega_{z,t}^2} + b,$$

In those expressions, ${}^i\omega_{x,t}$, ${}^i\omega_{y,t}$, and ${}^i\omega_{z,t}$ respectively stand for the gyroscope output for x , y , and z axes. Also a and b are adjusting parameters. For this study, a and b were determined to maximize the log-likelihood (iLL) shown in Eq. (22):

$$70 \quad {}^iLL = -\frac{N}{2} \ln(2\pi) - \frac{1}{2} \sum_{j=1}^N \left(\ln({}^iB_j) + \frac{{}^iV_j^2}{{}^iB_j} \right), \quad (22)$$

In that equation, N stands for the number of time-series data; j represents time-series. In addition, iB_j expresses the prediction error variance; iV_j signifies the prediction error.

The observation noise covariance matrices must be set at a high value when the sensor noise increases [32]. Therefore, the observation noise covariance matrix was determined based on the accelerometer and magnetometer output because the two sensor outputs were used as observation values [33]. The observation noise covariance matrix is presented below:

$$1 \quad {}^iR_t = \begin{bmatrix} {}^i\Omega_{m,t} & 0 & 0 & 0 \\ 0 & {}^i\Omega_{a,t} & 0 & 0 \\ 0 & 0 & {}^i\Omega_{a,t} & 0 \\ 0 & 0 & 0 & {}^i\Omega_{a,t} \end{bmatrix}, \quad (23)$$

2 where

$$3 \quad {}^i\Omega_{m,t} = c(\sqrt{{}^{c,i}m_{x,t}^2 + {}^{c,i}m_{y,t}^2 + {}^{c,i}m_{z,t}^2} - \bar{m}) + d,$$

$$4 \quad {}^i\Omega_{a,t} = e(\sqrt{{}^iA_{x,t}^2 + {}^iA_{y,t}^2 + ({}^iA_{z,t} - g)^2}) + f,$$

5
6 In the matrix, ${}^{c,i}m_{x,t}$, ${}^{c,i}m_{y,t}$, and ${}^{c,i}m_{z,t}$
7 respectively denote corrected magnetic field data for
8 the x , y , and z axes. In addition, \bar{m} represents the
9 average value of the magnetometer output over the
10 entire measurement time. Furthermore, ${}^iA_{x,t}$, ${}^iA_{y,t}$, and
11 ${}^iA_{z,t}$ respectively express the accelerometer outputs
12 for the x , y , and z axes. Therein, c , d , e , and f are
13 adjusting parameters. In addition, c , d , e , and f were
14 determined to maximize the log-likelihood (LL)
15 shown in Eq. (22). Several studies have proposed
16 process and observation noise covariance matrices
17 based on sensor output [33, 34]. In those earlier
18 studies, noise covariance matrices were produced
19 after calculating the deviation of each sensor using
20 many equations. The adjusting parameters a to f in the
21 noise covariance matrices are determined simply
22 using only log-likelihood calculations presented in Eq.
23 (22). In addition, interaction between the process
24 noise covariance and observation noise covariance is
25 considered in log-likelihood calculations.

26 The roll, pitch, and yaw angles in the
27 sensor i coordinate system obtained from the sensor
28 fusion are converted into the rotational matrix of the
29 reference coordinate system using Eq. (2). The lower
30 limb joint angles are calculated by substituting Eq. (2)
31 into Eq. (24) as shown below:
32

$$33 \quad {}^{i-1}R_i = ({}^0R_{i-1})^T \cdot ({}^0R_i), \quad (24)$$

34
35 In that equation, ${}^{i-1}R_i$ denotes the rotational matrix
36 from the sensor i coordinate system to the sensor $i-1$
37 system. The hip joint angle is estimated using the
38 output of the two sensors placed on the waist and
39 thigh. The knee joint angle is estimated using the
40 output of the two sensors placed on the thigh and
41 shank. The ankle joint angle is estimated using the
42 output of the two sensors positioned on the shank and
43 foot.

44 45 Verification experiment

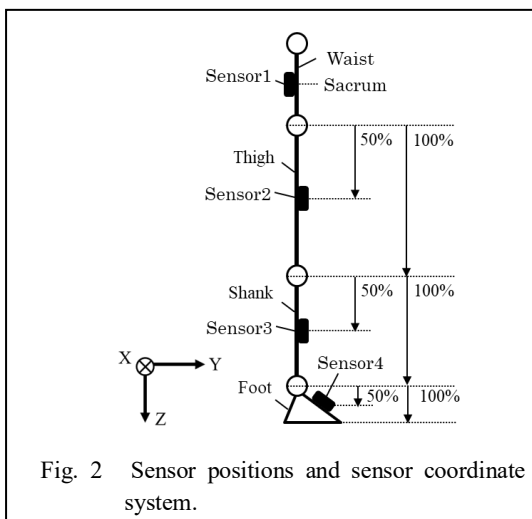
46 Participants and experiment conditions

47 Three healthy participants (A, B, and C) were
48 examined during the experiment. Anthropometric
49 data are shown in Table 1. After maintaining the
50 upright posture for about 5 s, the first step that a
51 participant took was with the left foot. They were
52 instructed to walk using a natural stride in time with
53 a metronome (70 bpm). Measurement started
54 simultaneously when a participant started to maintain
55 the upright posture. The measurements finished when
56 the participant placed the right foot flat on the floor
57 during the sixth step. Following an explanation of the
58 purpose and requirements of the study, the
59 participants gave their written informed consent to
60 participate in the study. Study approval was obtained
61 from the Research Ethics Board, Kogakuin University,
62 and National Institute of Technology, Akita College.

63 During the experiment, kinematic data
64 were collected using an optical 3D motion analysis
65 system (Bonita 10; Vicon Motion Systems Ltd.), two
66 force plates (9286; Kistler Japan Co. Ltd.), and four
67 nine-axis motion sensors in synchronization. The heel
68 strike and toe off were ascertained from force plate
69 data. The sensors were placed on the waist, left thigh,
70 left shank, and left foot using double-sided tape and
71 elastic straps. The sensor positions are presented in
72 Fig. 2. Definitions of the length of the thigh, shank,
73 and foot were referred from reports of earlier research

Table 1 Anthropometric data

Participant	Height [m]	Weight [kg]	Age [years]
A	1.78	60	20
B	1.72	65	20
C	1.80	56	21



1 [35]. Positions of reflective markers for the optical 3D
 2 motion analysis system were found by reference to 56
 3 the Vicon Plug-in Gait model. The sampling 57
 4 frequencies of the nine-axis motion sensors, the 58
 5 optical 3D motion analysis system, and the force 59
 6 plates were 100 Hz. 60

7 *Results* 62
 8 Table 2 shows parameters a to f in the walking 63
 9 experiment, which were found to maximize the log-64
 10 likelihood in Eq. (22). In the walking experiment, 65
 11 more or less equivalent parameters were obtained for 66
 12 all participants. 67

13 The joint angles of participant A are 68
 14 depicted in Fig. 3. Black solid curves represent 69
 15 results obtained from the optical 3D motion 70
 16 analysis system. Red solid curves represent 71
 17 results obtained from the extended Kalman 72
 18 filter using the noise covariance 73
 19 matrices based on sensor output, hereinafter 74
 20 designated as NBS. Orange solid curves represent 75
 21 results obtained from NBS, which used gyroscope 76
 22 output for the process noise covariance matrix and 77
 23 which used a constant value for the observation noise 78
 24 covariance matrix, hereinafter designated as NBS 79
 25 (Only process noise). Green solid curves represent 79
 26 results obtained from NBS, which used the constant 80
 27 value for the process noise covariance matrix and 81
 28 which used accelerometer and magnetometer output 82
 29 for the observation noise covariance matrix, 83
 30 hereinafter designated as NBS (Only observation 84
 31 noise). Blue solid curves present results obtained 85
 32 from the extended Kalman filter using the constant 86
 33 noise covariance, hereinafter designated as CNC. In 87
 34 addition, Ω_w (= 0.0005), Ω_m (= 1500), and Ω_a (= 88
 35 1500) of CNC were determined to maximize the log 89
 36 likelihood (LL) shown in Eq. (22). The horizontal 90
 37 axis shows the normalized time, where one gait cycle 91
 38 is 100%. One gait cycle in Fig. 3 extends from the 92
 39 beginning of the stance phase of the left leg (the third 93
 40 step) until the end of the swing phase. Table 3 shows 94
 41 root mean square errors (RMSE) between the 95
 42 estimated results and the results obtained from the 96
 43 3D motion analysis system. 97

44 Joint angles obtained from the three NBSs 98
 45 and CNC are generally consistent with the results 99
 46 obtained using the optical 3D motion analysis system. 100
 47 Results show the same tendency for joint angle 101
 48 variation as that found in an earlier study [35]. 102

49 The ankle joint angle obtained from NBS 103
 50 (Only process noise) is generally consistent with 104
 51 results obtained using the optical 3D motion analysis 105
 52 system at the dorsiflexion peak after toe-off. The 106
 53 ankle joint angle obtained from NBS (Only 107
 54 observation noise) is much smaller than the result 108

obtained from the optical 3D motion analysis system. The results indicate that the process noise covariance matrix based on the gyroscope output contributed to increased accuracy of the dorsiflexion peak during the swing phase.

In the early stance phase and the end of the swing phase, the ankle joint angle obtained from NBS (Only process noise) is much smaller than the result obtained from the optical 3D motion analysis system, whereas the ankle joint angle obtained from NBS (Only observation noise) is generally consistent with the result obtained using the optical 3D motion analysis system. The results indicate that the observation noise covariance matrix based on the accelerometer and magnetometer output contributed to increased accuracy at the early stance phase and at the end of the swing phase. Therefore, the process noise covariance matrix based on the gyroscope output and the observed noise covariance matrix based on the accelerometer and magnetometer output might have contributed to the increased accuracy at different phases.

For knee and hip joint angles, all results show the same tendency. However, NBS (red line) has the smallest RMSE in all results of all three joints. The results show that using both processes of noise covariance matrix based on the gyroscope output and the observed noise covariance matrix based on the accelerometer and magnetometer output might have contributed to increased accuracy. The two noise covariance matrices seem to have influenced one another.

Running experiment

Participants and experiment conditions

The nine-axis motion sensors measured lower limb joint angles of the same participants while they were running in place to verify the effectiveness of NBS when continuously capturing data of fast-moving participants. The nine-axis motion sensors were placed in the same positions as those used for the verification experiment. The measurement time was about 100 s. During the experiment, kinematic data were collected using an optical 3D motion analysis system with four nine-axis motion sensors in synchronization. Participants were instructed to run in place in time with a metronome (150 bpm) after maintaining the upright posture for about 5 s. The sampling frequencies of the nine-axis motion sensors and the optical 3D motion analysis system were 100 Hz.

Results

Table 4 shows parameters a to f for the running

Table 2 Adjusting parameters of NBS in the walking experiment.

(a) Ankle joint

Participant	Adjusting parameters					
	a	b	c	d	e	f
A	0.00001	0	0.1	0	1	0
B	0.00001	0	0.1	0	1	0
C	0.00001	0	0.1	0	1	0

(b) Knee joint

Participant	Adjusting parameters					
	a	b	c	d	e	f
A	0.00001	0	0.1	0	1	0
B	0.00001	0	0.1	0	1	0
C	0.00001	0	0.1	0	10	0

(c) Hip joint

Participant	Adjusting parameters					
	a	b	c	d	e	f
A	0.00001	0	0.1	0	1	0
B	0.00001	0	0.1	0	1	0
C	0.00001	0	0.1	0	10	0

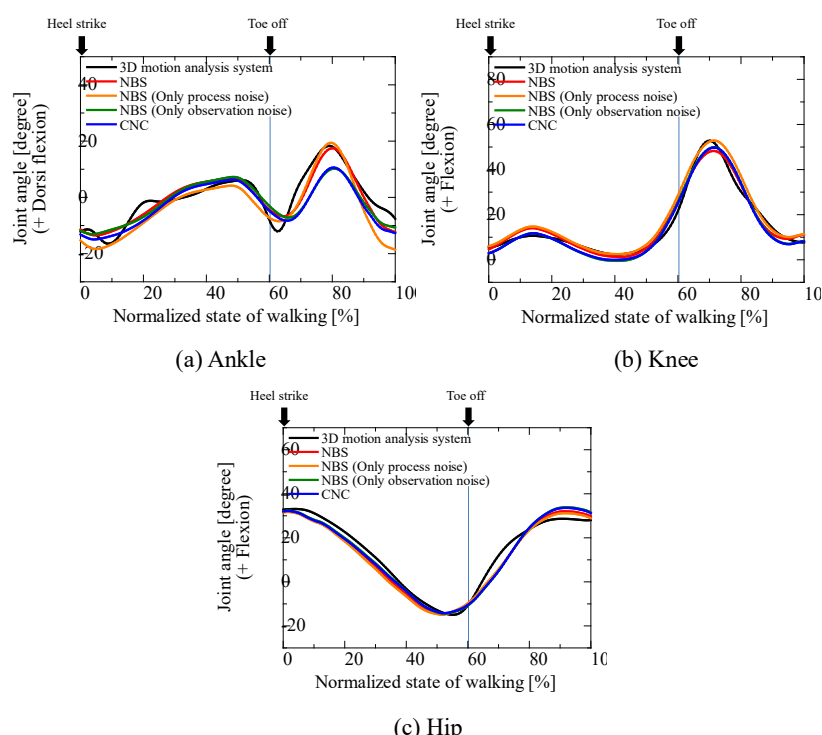


Fig. 3 Left lower limb joint angles during walking obtained using optical 3D motion analysis system, the extended Kalman filter using NBS, NBS (Only process noise), NBS (Only observation noise), and the extended Kalman filter using CNC (participant A).

Table 3 Root mean square errors for results obtained from two extended Kalman filters and 3D motion analysis system results (participant A).

Noise covariance matrix	RMSE [deg]		
	Ankle joint	Knee joint	Hip joint
NBS	3.17	2.41	3.18
NBS (Only process noise)	4.80	3.24	3.41
NBS (Only observation noise)	4.71	2.57	3.22
CNC	4.88	2.54	3.24

Table 4 Adjusting parameters of NBS in the running experiment.

(a) Ankle joint

Participant	Adjusting parameters					
	a	b	c	d	e	f
A	0.1	0	10	0	1000	0
B	0.1	0	10	0	1000	0
C	0.1	0	10	0	1000	0

(b) Knee joint

Participant	Adjusting parameters					
	a	b	c	d	e	f
A	0.00001	0	0.1	0	1	0
B	0.00001	0	100	0	100	0
C	0.00001	0	100	0	1000	0

(c) Hip joint

Participant	Adjusting parameters					
	a	b	c	d	e	f
A	0.1	0	10	0	1000	0
B	0.001	0	10	0	1000	0
C	0.001	0	10	0	1000	0

1 experiment, which were determined to maximize the 16
 2 log-likelihood in Eq. (22). From the running 17
 3 experiment, different parameters were obtained 18
 4 among the joints. In addition, parameters a , c , and e 19
 5 for running measurements tended to be larger than 20
 6 those in the walking measurement. The results 21
 7 indicate that the noise covariance matrices for the 22
 8 running experiment might have had larger values 23
 9 because the process and observation noise can 24
 10 increase if the motion velocity increases. 25
 11 The estimated joint angles of participant A 26
 12 are presented in Figs. 4, 5, and 6. In each of Figs. 4–27
 13 6, panels (a) present results obtained over the entire 28
 14 measurement time. Panels (b) present results obtained 29
 15 between 33 s and 35.5 s from the start of 30

measurements. In each of Figs. 4–6, panels (b) are used for a detailed examination of the results. Black solid curves present results obtained from the optical 3D motion analysis system. Red solid curves present results obtained from NBS. Blue solid curves present results obtained from CNC.

The estimated ankle joint angle using NBS in Fig. 4(a) changes periodically between -25° and 25° over the entire measurement time, which is generally consistent with results obtained using the optical 3D motion analysis system. The estimated ankle joint angle using CNC in Fig. 4(a) changes periodically between -70° and 0° over the entire measurement time. Although the waveform of the result obtained using CNC in Fig. 4(b) is similar to

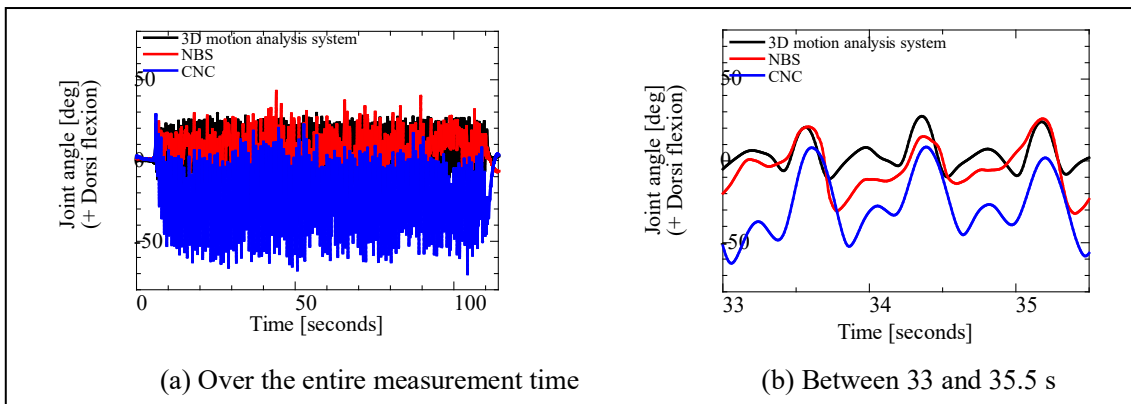


Fig. 4 Results obtained for ankle joint angles (Subject A).

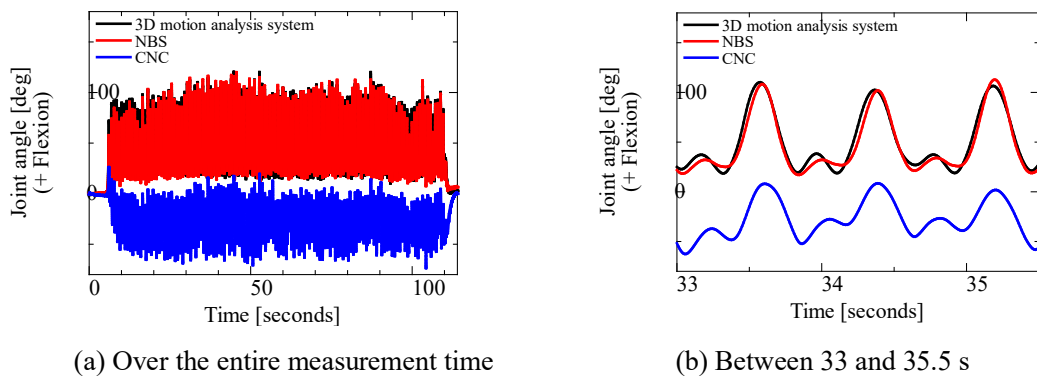


Fig. 5 Results obtained for knee joint angles (Subject A).

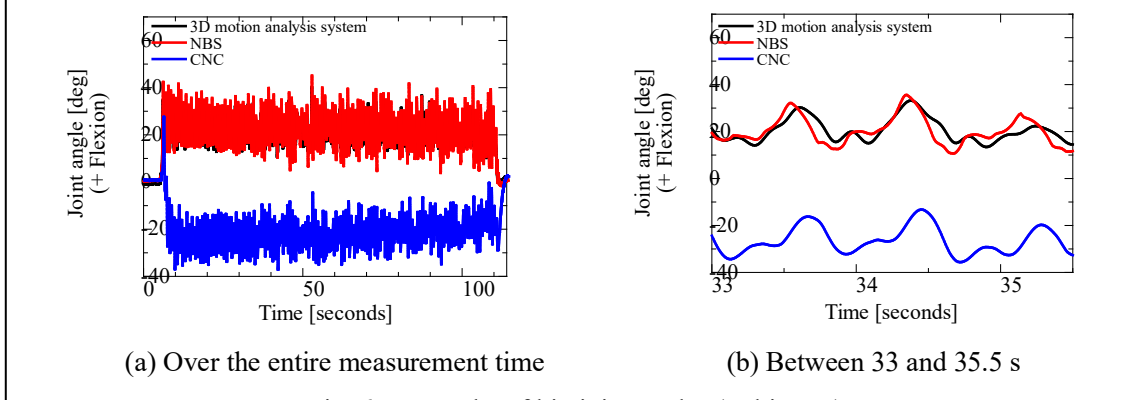


Fig. 6 Results of hip joint angles (Subject A).

1 the result obtained using NBS, the result obtained 11
 2 using CNC is much smaller than that obtained using 12
 3 NBS. Additionally, the waveform of the result 13
 4 obtained using CNC has a larger dorsiflexion peak 14
 5 than that obtained using NBS at about 33.7, 34.4, and 15
 6 35.2 s. 16
 7 The estimated knee joint angle obtained 17
 8 using NBS in Fig. 5(a) changes periodically between 18
 9 20° and 110° over the entire measurement time, 19
 10 which are generally consistent with the results 20
 obtained using the optical 3D motion analysis system.
 Whereas the estimated knee joint angle using CNC in
 Fig. 5(b) changes periodically between -60° and 0°
 over the entire measurement time. Although the
 waveform of the result obtained using CNC in Fig.
 5(b) is similar to the result obtained using NBS, the
 result obtained using CNC is much smaller than that
 obtained using NBS. Additionally, the waveform of
 the result obtained using CNC has a smaller flexion
 peak than that obtained using NBS at about 33.6,

1 34.35, and 35.2 s. 55
 2 The hip joint angle estimated using NBS 56
 3 in Fig. 6(a) changes periodically between 10° and 35° 57
 4 over the entire measurement time, which are 58
 5 generally consistent with results obtained using the 59
 6 optical 3D motion analysis system. The estimated 60
 7 knee joint angle using CNC in Fig. 6(a) changes 61
 8 periodically between -35° and -15° over the entire 62
 9 measurement time. Although the waveform of the 63
 10 result obtained using CNC in Fig. 6(b) is similar to 64
 11 the result obtained using NBS, the result obtained 65
 12 using CNC is much smaller than that obtained using 66
 13 NBS. All results obtained for the other two 67
 14 participants showed similar tendencies. The results 68
 15 demonstrated the effectiveness of the extended 69
 16 Kalman filter using NBS. 70
 17 71
18 Conclusions 72
 19 For this study, a method for ascertaining the process 73
 20 and observation noise covariance matrices in the 74
 21 extended Kalman filter based on sensor output was 75
 22 constructed to estimate the lower limb joint angles. 76
 23 The lower limb joint angles of the three healthy 77
 24 participants during walking and running were 78
 25 estimated using the method. Results yielded the 79
 26 following conclusions. 80
 27 81
 28 1. The joint angles obtained from the extended 82
 29 Kalman filter using the process and observation noise 83
 30 covariance matrices based on sensor output were 84
 31 generally consistent with results obtained using the 85
 32 optical 3D motion analysis system in the verification 86
 33 experiment. 87
 34 2. In the running motion analysis, the results obtained 88
 35 using noise covariance matrices based on sensor 89
 36 output indicated that the estimated joint angles 90
 37 changed periodically within an appropriate range. 91
 38 The results obtained using the constant noise matrices 92
 39 covariance indicated that the estimated joint angles 93
 40 changed abnormally. 94
 41 95
 42 Noise covariance matrices based on sensor 96
 43 output can be effective for accurate pose estimation 97
 44 because noise covariance matrices can be time- 98
 45 variable when continuously capturing human motion 99
 46 with long-term measurements. The proposed method 100
 47 is expected to be useful for estimating motion in 101
 48 sports and healthcare applications. 102
 49 103
50 Competing interests 104
 51 The authors declare that they have no competing 105
 52 interests. 106
 53 107
54 Funding 108

This work was supported by JSPS KAKENHI Grant Number JP 20K19588.

Authors' Contributions

AS conceived the study and drafted the manuscript. AS and KM carried out all experiments and analyzed the data. YK and SK participated in the research design and sequence alignment. All authors read and approved the final manuscript.

Acknowledgments

Not applicable

Author details

Department of Mechanical Science and Engineering,
 Kogakuin University
 2665-1 Nakanomachi, Hachioji, Tokyo 192-0015,
 Japan
 Ayuko SAITO

Department of Mechanical Engineering and Robotics,
 National Institute of Technology (KOSEN), Akita
 College, 1-1 Iijima-Bunkyo-cho, Akita 011-8511,
 Japan
 Satoru KIZAWA, Yoshikazu KOBAYASHI and
 Kazuto MIYAWAKI

Corresponding author

Correspondence to Ayuko SAITO.

E-mail of corresponding author:
 saito@cc.kogakuin.ac.jp

References

- King, K., Yoon, S. W., Perkins, N. C. and Najaf, K., Wireless MEMS inertial sensor system for golf swing dynamics, *Sensors and Actuators A: Physical*, Vol.141, No. 2 (2008), pp.619–630.
- Favre, J., Aissaoui, R., Jolles, B. M., Guise, J. A. and Aminian, K., Functional calibration procedure for 3D knee joint angle description using inertial sensors, *Journal of Biomechanics*, Vol.42, No. 14 (2009), pp.2330–2335.
- Ameli, S., Naghdly, F., Stirling, D., Naghdly, G. and Aghmesheh, M., Objective clinical gait analysis using inertial sensors and six minute walking test, *Pattern Recognition*, Vol.63 (2017), pp.246–257.
- Nüesch, C., Roos, E., Pagenstert, G. and Mündermann, A., Measuring joint kinematics of treadmill walking and running: Comparison between an inertial sensor based system and a camera-based system, *Journal of Biomechanics*, Vol.57 (2017), pp.32–38.
- Kruk, E., Schwab, A. L., Helm, F. C. T. and Veeger, H. E. J., Getting in shape: Reconstructing three-

- dimensional long-track speed skating kinematics by comparing several body pose reconstruction techniques, *Journal of Biomechanics*, Vol.69, No. 5 (2018), pp.103–112. 55
6. Bavan, L., Surmacz, K., Beard, D., Mellon, S. and Rees, J., Adherence monitoring of rehabilitation exercise with inertial sensors: A clinical validation study, *Gait & Posture*, Vol.70 (2019), pp.211–217. 60
7. Hullfish, T. J., Qu, F., Stoeckl, B. D., Gebhard, P. M., Mauck, R. L. and Baxter, J. R., Measuring clinically relevant knee motion with a self-calibrated wearable sensor, *Journal of Biomechanics*, Vol.89, No. 24 (2019), pp.105–109. 64
8. Nazarabari, M., Noamani, A., Ahmadian, N. and Rouhani, H., Sensor-to-body calibration procedure for clinical motion analysis of lower limb using magnetic and inertial measurement units, *Journal of Biomechanics*, Vol.85, No. 6 (2019), pp.224–229. 68
9. Hirose, K., Doki, H., Koda, S. and Nagasaku, K., Studies of the dynamic analysis and motion measurement of skiing turn using extended Kalman filter, *Transactions of the Japan Society of Mechanical Engineers, Series C*, Vol.77, No. 77478 (2011), pp.470–480 (in Japanese). 72
10. Chardonnens, J., Favre, J., Cuendet, F., Gremion, G. and Aminian, K., A system to measure the kinematics during the entire ski jump sequence using inertial sensors, *Journal of Biomechanics*, Vol.46, No. 1 (2013), pp.56–62. 76
11. Hirose, K., Doki, H. and Kondo, A., Studies of orientation measurement in sports using inertial and magnetic field sensors, *Japan Society of Sports Industry*, Vol.22, No. 2 (2012), pp.255–262 (in Japanese). 80
12. Saito, A., Miyawaki, K., Kizawa, S. and Kobayashi, Y., A study of estimating the knee joint angle during walking using the motion sensors (Focusing on the effect of centrifugal acceleration and tangential acceleration), *Transactions of the JSME*, Vol.84, No. 857 (2018a), DOI: 10.1299/transjsme.17-00488 (in Japanese). 84
13. Saito, A., Miyawaki, K., Komatsu, A. and Iwami, T., A study of sensor position for thigh and lower leg motion sensors during walking (Focusing on the knee sagittal plane angle), *Transactions of the JSME*, Vol.84, No. 865 (2018b), DOI: 10.1299/transjsme.18-00263 (in Japanese). 88
14. Kondo, A., Doki, H. and Hirose, K., A study of calibration method of magnetic field sensor for body motion measurement using inertial sensors, *Proceedings of the Sports Engineering and Human Dynamics* (2013), DOI: 10.1299/jsmeshd.2013_212-1 (in Japanese). 92
15. Saito, A., Nara, Y. and Miyawaki, K., A study of estimating knee joint angle using motion sensors under conditions of magnetic field variation, *Transactions of the JSME*, Vol.85, No. 873 (2019), DOI: 10.1299/transjsme.19-00061 (in Japanese). 96
16. Rigatos, G. G., Extended Kalman and Particle Filtering for sensor fusion in motion control of mobile robots, *Mathematics and Computers in Simulation*, Vol.81, No. 3 (2010), pp.590–607. 100
17. Adachi, S. and Maruta, I., Fundamentals of Kalman filter (2012), pp. 95–111, Tokyo Denki University Press (in Japanese). 104
18. Ran, C. and Deng, Z., Self-tuning weighted measurement fusion Kalman filtering algorithm, *Computational Statistics & Data Analysis*, Vol.56, No. 6 (2012), pp.2112–2128. 108
19. Kamil, M., Chobtrong, T., Günes, E. and Haid, M., Low-cost object tracking with MEMS sensors, Kalman filtering and simplified two-filter-smoothing, *Applied Mathematics and Computation*, Vol.235 (2014), pp.323–331. 112
20. Zheng, Z., Qiu, H., Wang, Z., Luo, S. and Lei, Y., Data fusion based multi-rate Kalman filtering with unknown input for on-line estimation of dynamic displacements, *Measurement*, Vol.131 (2019), pp.211–218. 116
21. Baerveldt, A. J. and Klang, R., A low-cost and low-weight attitude estimation system for an autonomous helicopter, *Proceedings of IEEE International Conference on Intelligent Engineering Systems* (1997), pp.391–395. 120
22. Mahony, R., Hamel, T. and Pflimlin, J. M., Complementary filter design on the special orthogonal group SO(3), *Proceedings of the 44th IEEE Conference on Decision and Control, and the European Control Conference 2005* (2005), pp.1477–1484. 124
23. Euston, M., Coote, P., Mahony, R., Kim, J. and Hamel, T., A complementary filter for attitude estimation of a fixed-wing UAV, *Proceedings of 2008 IEEE/RSJ International Conference of Intelligent Robots and Systems* (2008), pp.340–345. 128
24. Mahony, R., Hamel, T. and Pflimlin, J. M., Nonlinear complementary filters on the special orthogonal group, *IEEE Transactions on Automatic Control*, Vol.53, No. 5 (2008), pp.1203–1218. 132
25. Sugihara, T., Masuya, K. and Yamamoto, M., A complementary filter for high-fidelity attitude estimation based on decoupled linear/nonlinear properties of inertial sensors, *Journal of the Robotics Society of Japan*, Vol.31, No. 3 (2013), pp.251–262 (in Japanese). 136

- 1 26. Aoki, K., The brand-new technology: Motion
2 analysis system, Journal of the Society of
3 Biomechanisms, Vol.32, No. 3 (2008), pp.167–172
4 (in Japanese).
- 5 27. Ehara, Y., The VICON, Journal of the Society of
6 Biomechanisms, Vol.32, No. 2 (2008), pp.107–111
7 (in Japanese).
- 8 28. Syam, P. N., Sheila, G., Graham, A., Rami, A. and
9 Weijie, W., A method to calculate the centre of the
10 ankle joint: A comparison with the Vicon® Plug-
11 in-Gait model, Clinical Biomechanics, Vol.25, No.
12 6 (2010), pp.582–587.
- 13 29. Stief, F., Böhm, H., Michel, K., Schwirtz, A. and
14 Döderlein, L., Reliability and accuracy in three-
15 dimensional gait analysis: A comparison of two
16 lower body protocols, Journal of Applied
17 Biomechanics, Vol.29 (2013), pp.105–111.
- 18 30. Vaganay, J., Aldon, M. J. and Fournier, A., Mobile
19 robot attitude estimation by fusion of inertial data,
20 Proceedings of the IEEE International Conference
21 on Robotics and Automation (1993), pp.277–282.
- 22 31. Jurman, D., Jankovec, M., Kamnik, R. and Topic,
23 M., Calibration and data fusion solution for the
24 miniature attitude and heading reference system,
25 Sensors and Actuators A: Physical, Vol.138, No. 2
26 (2007), pp.411–420.
- 27 32. Hirose, K. and Kondo, A., Special Issues No. 3:
28 Measurement Technique for Ergonomics, The
29 Japanese Journal of Ergonomics, Vol.50, No. 4
30 (2014), pp.182–190 (in Japanese).
- 31 33. Miyamoto, G., Sonobe, M., Shibata, K. and
32 Hirose, K., Development of gait measurement
33 system using IMU sensors, Proceedings of the
34 Chugoku and Shikoku Regional Conference
35 (2019), DOI: 10.1299/jsmechs.2019.57.1001 (in
36 Japanese).
- 37 34. Jurman, D., Jankovec, M., Kamnik, R. and Topic,
38 M., Calibration and data fusion solution for the
39 miniature attitude and heading reference system,
40 Sensors and Actuators A: Physical, Vol.138, No. 2
41 (2007), pp.411–420.
- 42 35. Ae, M., Tang, H. and Yokoi, T., Estimation of
43 inertia properties of the body segments in Japanese
44 athletes, Biomechanism, Vol.11 (1992), pp.23–33
45 (in Japanese).
- 46 36. Yamamoto, H. and Yanagida, Y., The various
47 patterns of knee angle in the stance phase, The
48 Society of Physical Therapy Science, Vol.26, No. 2
49 (2011), pp.269–273 (in Japanese).

Figures

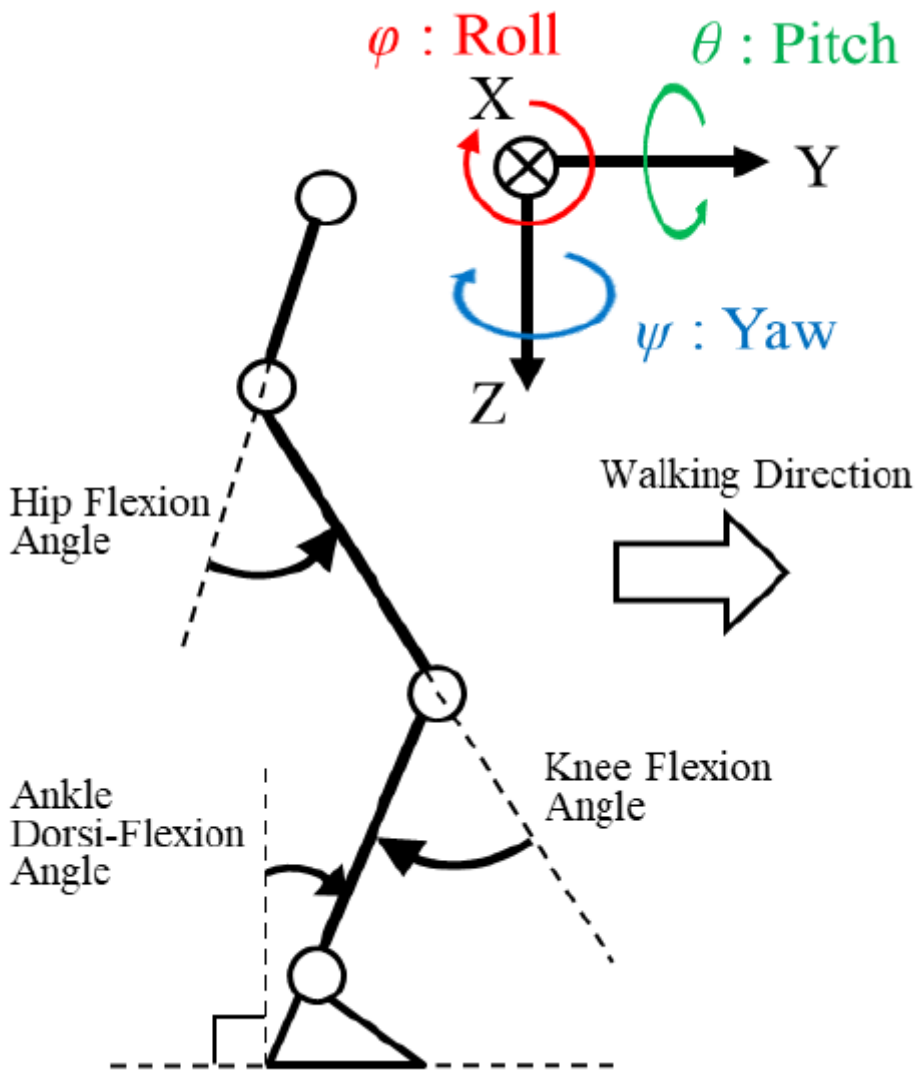


Figure 1

Definition of the lower limb joint angles and the reference coordinate system.

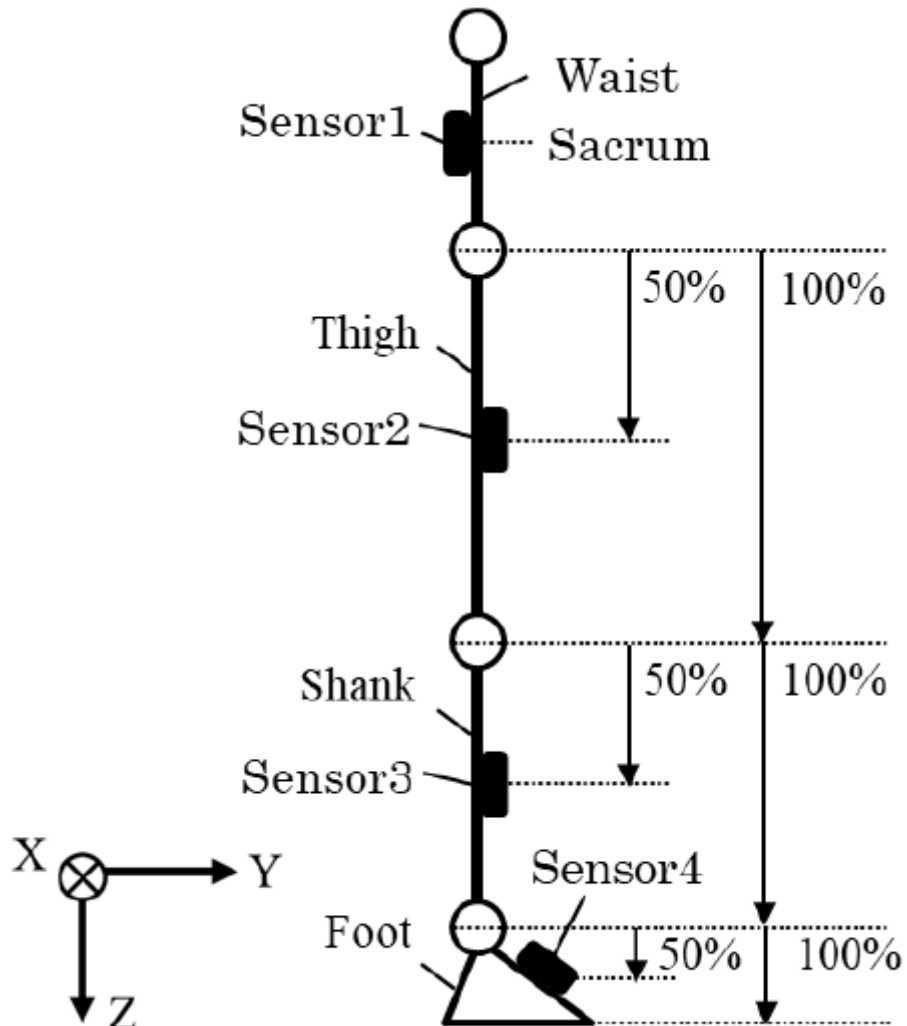
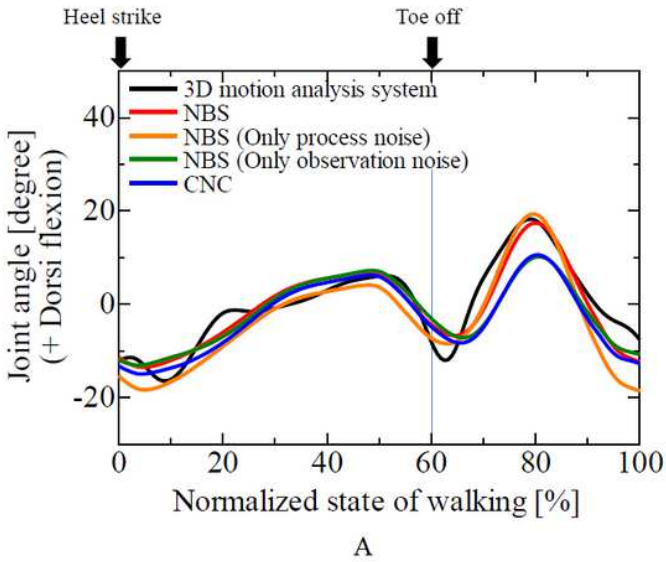
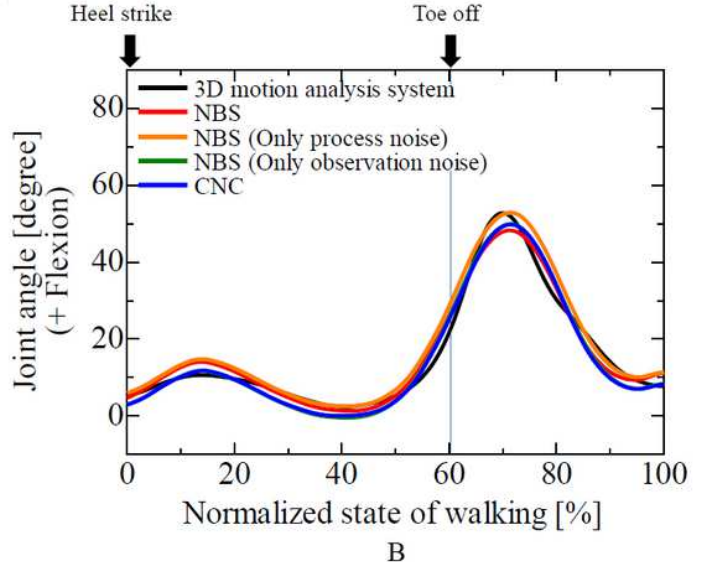


Figure 2

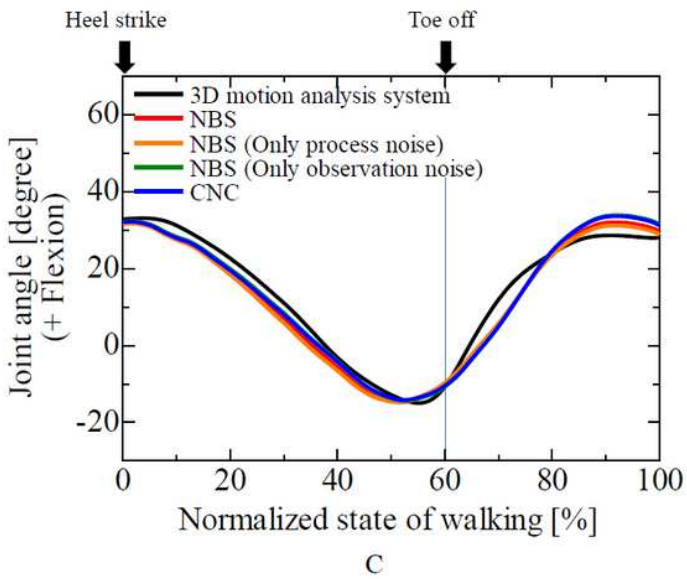
Sensor positions and sensor coordinate system.



A



B



C

Figure 3

Left lower limb joint angles during walking obtained using optical 3D motion analysis system, the extended Kalman filter using NBS, NBS (Only observation noise), NBS (Only process noise), and the extended Kalman filter using CNC (participant A). (a) Ankle (b) Knee (c) Hip

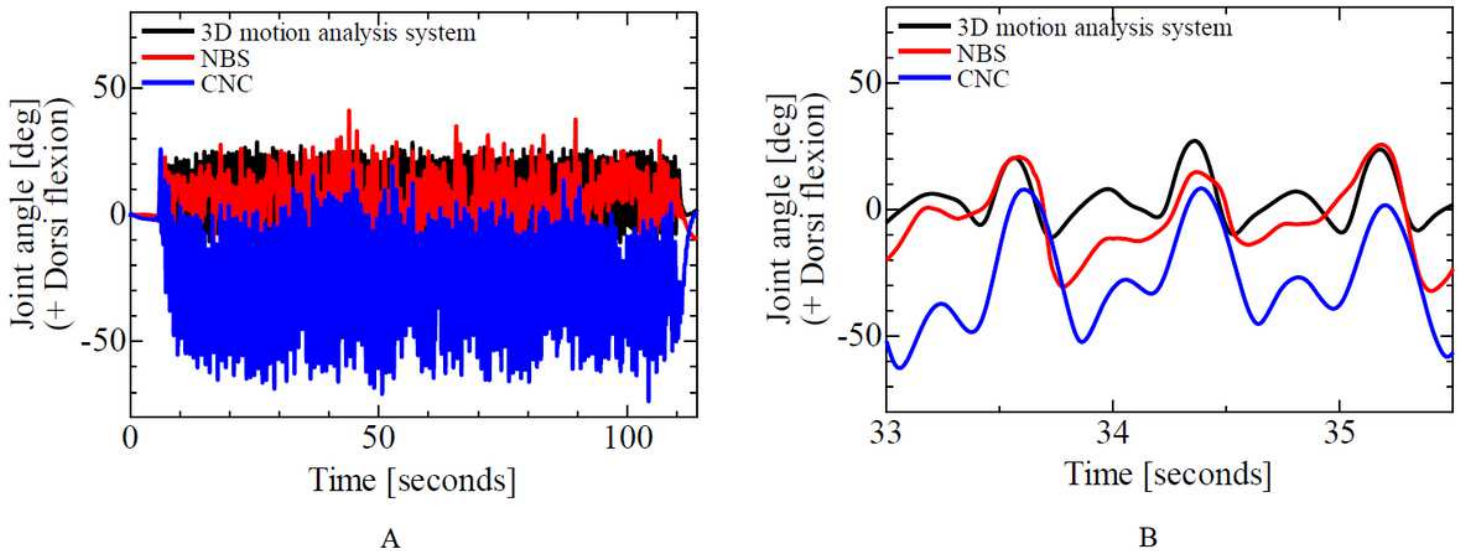


Figure 4

Results obtained for ankle joint angles (Subject A). (a) Over the entire measurement time (b) Between 33 and 35.5 s

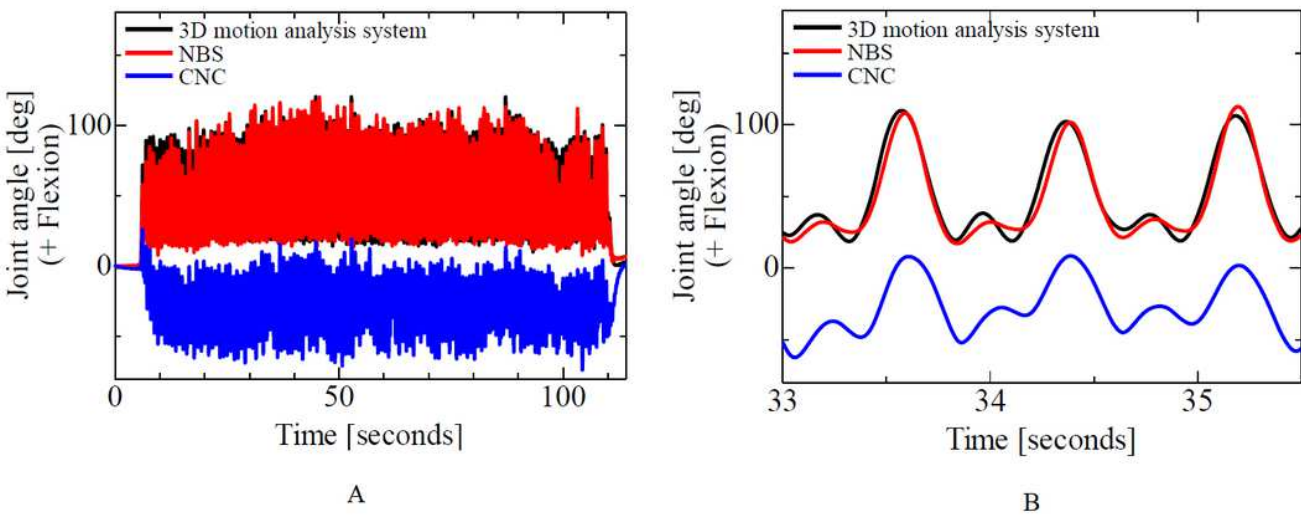
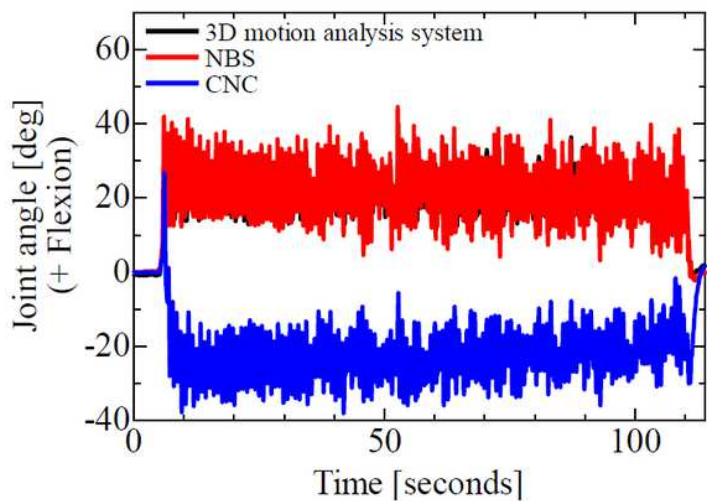
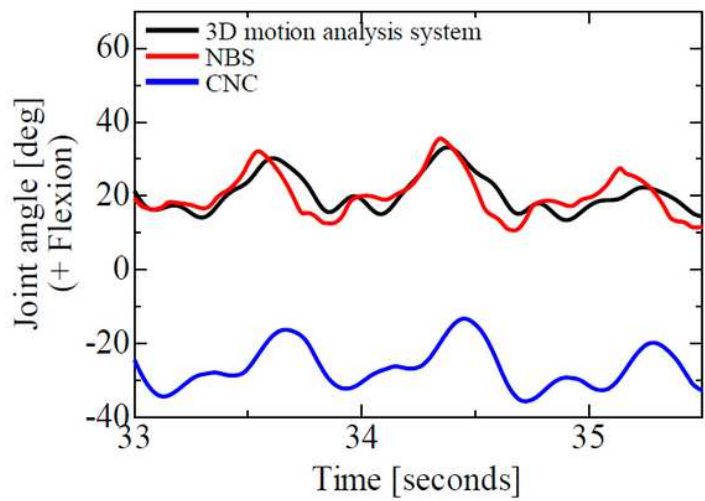


Figure 5

Results obtained for knee joint angles (Subject A). (a) Over the entire measurement time (b) Between 33 and 35.5 s



A



B

Figure 6

Results of hip joint angles (Subject A). (a) Over the entire measurement time (b) Between 33 and 35.5 s